

Searching for dark neutrinos through exotic Higgs decays at the ILC

Simon Thor

KTH Royal Institute of Technology, 100 44 Stockholm, Sweden

Masaya Ishino and Junping Tian

International Center for Elementary Particle Physics,

The University of Tokyo, Tokyo 113-0033, Japan

(Dated: September 21, 2023)

In this study we investigate the feasibility of detecting heavy dark neutrinos (N_d) through exotic Higgs decays at the proposed International Linear Collider (ILC), specifically in the channel of $e^+e^- \rightarrow qq H$ with $H \rightarrow \nu N_d \rightarrow \nu lW \rightarrow \nu l qq$. Analyses based on full detector simulations of the ILD are performed at the center-of-mass energy of 250 GeV for two different beam polarization schemes with a total integrated luminosity of 2 ab^{-1} . A range of dark neutrino masses between the Z boson and Higgs boson masses are studied. The 2σ significance reach for the joint branching ratio of $BR(H \rightarrow \nu N_d) \cdot BR(N_d \rightarrow lW)$ is about 0.1%, nearly independent of the dark neutrino masses, while the 5σ discovery is possible at a branching ratio of 0.3%. Interpreting these results in terms of constraints on the mixing parameters $|\varepsilon_{id}|^2$ between SM neutrinos and the dark neutrino, it is expected to have a factor of 10 improvement from current constraints.

I. INTRODUCTION

The discovery of the Higgs boson at the Large Hadron Collider (LHC) [1, 2] marked a monumental milestone in the field of particle physics, confirming the existence of the Higgs field and adding the final puzzle piece to the Standard Model. However, there are still gaping holes in particle physics that cannot be answered by the Standard Model, including the existence of dark matter, matter-antimatter asymmetry and more. Physics beyond the Standard Model (BSM) is therefore a necessity. Despite this, no clear signs of BSM physics have so far been found. However, the Higgs boson with its unique properties and being the

least understood particle in the Standard Model, hosts great potential for being a portal to explore BSM physics. By measuring the Higgs boson properties precisely, it is possible that BSM physics could be discovered [3].

In this paper, we investigate the sensitivity of the International Linear Collider (ILC) [4] in detecting dark neutrinos as an exotic decay product of the Higgs boson, motivated by the model proposed in [5] to explain the matter-antimatter asymmetry problem. Our study leverages full detector simulations of the International Large Detector (ILD) [6]. We consider a range of dark neutrino masses and branching ratios. In the subsequent sections of this paper, we discuss the theoretical framework and models considered, outline the details of the accelerator and the detector, present the methodology employed, present the results of our analysis, and conclude with a summary of our findings and their implications.

A. Theoretical framework

In [5], baryogenesis is achieved by a model that adds a dark sector to the SM, where the first-order phase transition as well as CP-violation happen only in the dark sector and the asymmetry is converted to the SM baryon asymmetry by employing a renormalizable neutrino portal Yukawa interaction,

$$\Delta\mathcal{L}_Y = -y_{i\alpha}\bar{l}_i N_\alpha \tilde{H} + c.c., \quad (1)$$

where N_α ($\alpha = u, d$) are the two singlet dark neutrinos, $\tilde{H} = i\sigma_2 H^*$, where H is the SM Higgs doublet, l_i ($i = e, \mu, \tau$) are the SM lepton doublets, and $y_{i\alpha}$ are the corresponding Yukawa coupling constants. This Yukawa interaction generates a mixing between the SM neutrinos and dark neutrinos with the corresponding mixing parameter ε_{iu} or ε_{id} , which determines the coupling strength between dark neutrinos and SM particles Higgs, W and Z bosons. In our study we focus on the search of N_d only which is expected to have a mass at around electroweak scale, thus accessible at the ILC, while the mass of N_u is expected to be much higher.

The two free parameters in this model that are relevant for this study are thus the dark neutrino mass m_N (for N_d) and the mixing parameter ε_{id} . At colliders N_d can be produced directly, as shown in Figure 1 for a representative Feynman diagram at e^+e^- . This would be the major method to search for the dark neutrino when it is heavy [7].

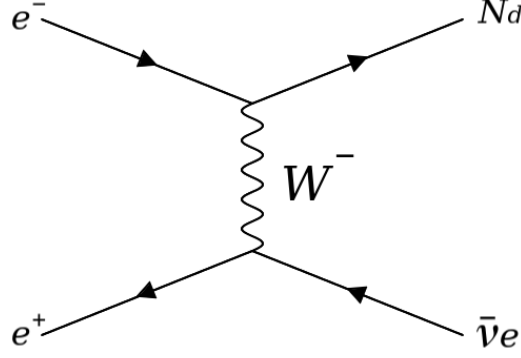


FIG. 1: Direct production of dark neutrinos through e^+e^- collisions. It is also possible to have the same diagram but with swapped SM and dark neutrinos and exchanging

$$\bar{\nu}_e \rightarrow \nu_e, N_d \rightarrow \bar{N}_d.$$

When its mass is below Z or W it is possible to search it via the decay of Z or W . When the dark neutrino is just heavier than Z but lighter than Higgs, an interesting method is enabled by searching for the dark neutrino from Higgs exotic decay. This is exactly the range of dark neutrino masses that we focus on in this study. The corresponding decay widths in terms of the two free parameters are given below

$$\Gamma(H \rightarrow \bar{\nu}_j N_d) = \left(\frac{|\varepsilon_{jd}| m_N}{v} \right)^2 \beta_f(m_H, m_N)^2 \frac{m_H}{4\pi} \equiv C_H |\varepsilon_{jd}|^2 \quad (2)$$

$$\Gamma(N_d \rightarrow l_i^- W^+) = \frac{(|\varepsilon_{id}| g)^2}{32\pi} \beta_f(m_H, m_N)^2 \frac{m_N^3}{m_W^2} \left(1 + 2 \left(\frac{m_W}{m_N} \right)^2 \right) \equiv C_W |\varepsilon_{id}|^2 \quad (3)$$

$$\Gamma(N_d \rightarrow \nu_i Z) = \frac{(|\varepsilon_{id}| g)^2}{64\pi} \beta_f(m_H, m_N)^2 \frac{m_N^3}{m_W^2} \left(1 + 2 \left(\frac{m_Z}{m_N} \right)^2 \right) \equiv C_Z |\varepsilon_{id}|^2 \quad (4)$$

Here, v is the vacuum expectation value 246 GeV, $\beta_f(M, m) = 1 - (m/M)^2$, g is the electroweak $SU(2)$ coupling constant, m_W is the W boson mass, and m_Z is the Z boson mass, and i, j indicate the lepton flavor. The equations are slightly modified versions of the ones given in [8]. We have defined C_H, C_W, C_Z as the product of all terms that depends on the dark neutrino mass instead of the mixing parameter. The charge conjugate decay mode $H \rightarrow \nu_j \bar{N}_d$ is of course also possible, with the corresponding decays $N_d \rightarrow l_i^+ W^-$ and $N_d \rightarrow \bar{\nu}_i Z$.

Given above theory basis we are ready to define our signal process at the ILC. We will take advantage of the leading Higgs production channel (Higgs-strahlung process) $e^+e^- \rightarrow ZH$

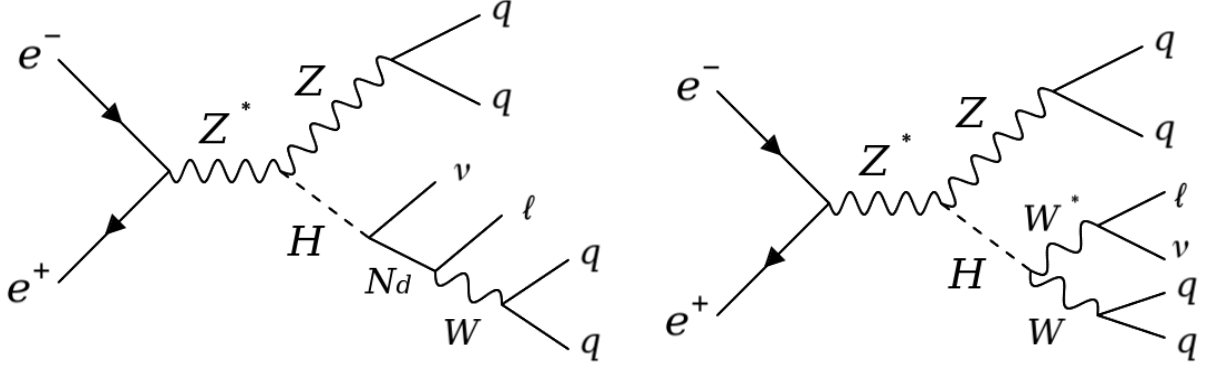


FIG. 2: Feynman diagrams for the signal (left) and the main background (right) in this study.

and look for the Higgs exotic decay mode $H \rightarrow \bar{\nu} N_d$. We will concentrate on the dominant decay channel where $Z \rightarrow q\bar{q}$ and $N_d \rightarrow l^- W^+ \rightarrow l^- q\bar{q}$. The charge conjugate channel is also targeted as our signal process. The Feynman diagram of this signal process is shown in Figure 2 (left). The observable will be the event rate of the signal process, which is basically the product of the cross section of $e^+e^- \rightarrow ZH$ cross section (σ_{ZH}) and decay branching ratios (BR) of $Z \rightarrow q\bar{q}$, $H \rightarrow \bar{\nu} N_d$, $N_d \rightarrow l^- W^+$ and $W \rightarrow q\bar{q}$. With σ_{ZH} , $BR(Z \rightarrow q\bar{q})$ and $BR(W \rightarrow q\bar{q})$ precisely measured in other processes at the ILC, the observable here essentially becomes a joint branching ratio of H and N_d decays, $BR(H \rightarrow \bar{\nu} N_d) \cdot BR(N_d \rightarrow l^- W^+)$, which can be computed as a function of the two free parameters m_N and ε_{id} as follows (using equations 2, 3, 4)

$$\begin{aligned}
 & \sum_j BR(H \rightarrow \bar{\nu}_j N_d) \cdot BR(N_d \rightarrow l_i^- W^+) \\
 &= \frac{\sum_j \Gamma(H \rightarrow \bar{\nu}_j N_d)}{\Gamma_{SM} + \sum_j \Gamma(H \rightarrow \bar{\nu}_j N_d)} \frac{\Gamma(N_d \rightarrow l_i^- W^+)}{\sum_k (\Gamma(N_d \rightarrow l_k^- W^+) + \Gamma(N_d \rightarrow \nu_k Z))} \\
 &= \frac{\sum_j |\varepsilon_{jd}|^2 C_H}{\Gamma_{SM} + \sum_j |\varepsilon_{jd}|^2 C_H} \frac{C_W |\varepsilon_{id}|^2}{\sum_j (|\varepsilon_{jd}|^2 C_W + |\varepsilon_{jd}|^2 C_Z)} = \frac{C_H}{\Gamma_{SM} + \sum_j |\varepsilon_{jd}|^2 C_H} \frac{C_W |\varepsilon_{id}|^2}{C_W + C_Z} \\
 &\approx \frac{C_H}{\Gamma_{SM}} \frac{C_W}{C_W + C_Z} |\varepsilon_{id}|^2,
 \end{aligned} \tag{5}$$

where the approximation in the last step holds when the decay width contribution to the Higgs from the dark neutrino is far smaller than the Higgs SM decay width Γ_{SM} . Equation 5 tells that the observable defined above for the channel with l_i is proportional to the

corresponding mixing parameter squared ε_{id} . More explicitly, when the charged lepton in the final state is e the observable depends simply on ε_{ed} instead of a combination of ε_{ed} , $\varepsilon_{\mu d}$ and $\varepsilon_{\tau d}$. Numerically, for our interested mass range $m_Z < m_N < m_H$, $\frac{C_W}{C_W+C_Z}$ is $O(1)$ ($> 75\%$, closer to 1 for smaller m_N), and $\frac{C_H}{\Gamma_{SM}}$ is $O(10)$.

1. Current constraints

It's worth summarizing here current constraints on the two free parameters in above model. First of all as given in [5], based on the test of lepton universality [9] $|\varepsilon_{id}|^2$ is typically constrained to $|\varepsilon_{id}|^2 \lesssim 10^{-3}$. This constraint is independent of the dark neutrino mass. In the mass range below m_Z , the constraint from Z decay comes from DELPHI at LEP1 [10]. For short-lived heavy neutral leptons, when $m(N_d)$ is between 5 and 50 GeV, the constraint can be as strong as $\varepsilon \lesssim 2 \times 10^{-5}$, while it is weaker when $m_N > 50$ GeV. The constraints from searches of heavy neutral leptons at the LHC experiments [11, 12] can also be cast into the parameters defined here, notably in the mass range well below m_W ($\lesssim 10$ GeV) the limit on $|\varepsilon_{id}|^2$ can be as strong as 10^{-6} if the heavy neutrino is long-lived and therefore has a displaced vertex.

For the mass range we are interested in this study, there is no stronger limit yet from current LHC experiments. According to [8], the measurement of Higgs total width at the LHC can set an indirect limit which is very weak at this moment; stronger limit might be possible using Higgs exotic decay but leptonic final state $H \rightarrow \nu N_d \rightarrow ll\nu\nu$, based on DELPHES fast detector simulation.

It is interesting to note another method which can give indirect limit. At parton level, Higgs SM decay to WW^* can give exactly same final states as Higgs exotic decay to νN_d , illustrated in Figure 2 (right). Thus the measurement of $H \rightarrow WW^*$ branching ratio can provide a constraint on $BR(H \rightarrow \nu N_d)$ if the event selection efficiency for $H \rightarrow \nu N_d$ events is not zero in the $H \rightarrow WW^*$ analysis. The current measurements of the branching ratio is $BR(H \rightarrow WW^*) = 25.7 \pm 2.5\%$ [13]. Assuming that all of $H \rightarrow \nu N_d$ decays contribute to the $H \rightarrow WW^*$ decay channel, the 2σ limit for the branching ratio of $H \rightarrow \nu N_d$ is 5%. This constraint on the branching ratio is overly optimistic but is nevertheless included as a comparison.

All of the above mentioned constraints are shown in the results section and compared to

the ILC constraints.

II. SIMULATION FRAMEWORK

A. International Linear Collider

The International Linear Collider (ILC) is a proposed future linear e^+e^- collider. One of the main goals of the collider is to be a Higgs factory, i.e., produce Higgs bosons and perform precision measurements of its properties. The hope is that some of these properties will deviate from predictions by the SM and will therefore be a hint of BSM, as explained earlier. The center-of-mass energy is planned to be 250 GeV at the start, with possibilities to extend the accelerator and thus increasing the collision energy in later stages. At 250 GeV, the cross section for Higgsstrahlung process, i.e., $e^+e^- \rightarrow ZH$ (see Feynman diagrams in Figure 2) reaches its maximum value and is therefore a suitable center-of-mass energy to perform measurements of the Higgs. The latest overviews of ILC can be found in the ILC documents for the Snowmass 2022 [3] and European Strategy Update for HEP 2020 [14]. Our study is assuming a total integrated luminosity of 2 ab^{-1} at the ILC $\sqrt{s} = 250$ GeV, equally shared among two beam polarization schemes: $P(e^-, e^+) = (-0.8, +0.3)$ and $P(e^-, e^+) = (+0.8, -0.3)$ [15].

B. The ILD concept

Our full detector simulation is based on the ILD which is one of the two proposed detectors for the ILC. It has a hybrid tracking system and highly granular calorimeters optimized for Particle Flow reconstruction. It has been developed to be optimized for precision measurements of the Higgs boson, the weak gauge bosons and the top-quark, as well as for direct searches of new particles [6]. The subdetectors relevant for this study are briefly described below.

The vertexing system consists of three double layers of silicon pixel detectors and is located closest to the interaction point. Each layer has a spatial resolution of $3 \mu\text{m}$ and a timing resolution per layer of 2-4 μs or potentially lower. The hybrid tracking system consists of both a silicon strip detector and a time projection chamber (TPC). The silicon detectors are placed before and after the TPC. The whole tracking system is located outside

the vertexing system. The TPC allows for up to 220 three-dimensional points and a spatial resolution lower than $100 \mu\text{m}$ for each hit and can also identify particle types from the dE/dx energy loss. The silicon strips enable further improvements to the track momentum resolution. With this setup, charged particle momenta can be measured down to $\frac{\delta p_t}{p_t^2} = 2 \times 10^{-5} \text{ GeV}^{-1}$.

The electromagnetic calorimeter (ECAL), located outside the tracking system, is a sampling calorimeter made out of silicon and tungsten in finely segmented pads of $(5 \times 5) \text{ mm}^2$. A shower can be sampled up to 30 times and give a timing resolution of 100 ps or better. The hadronic calorimeter is located outside the ECAL and is based on scintillator as default consisting of $(3 \times 3) \text{ cm}^2$ tiles. High-performance and high-resolution calorimeters are crucial for particle flow, as every particle in each jet is separated and reconstructed.

Outside of the calorimeters there is a superconducting solenoid with a magnetic field of 3.5 T. An iron return yoke located outside the coil works as a muon identification system. The muon detector is scintillator-based and is mostly located in the inner half of the iron yoke.

C. Software

This study utilizes the software package ILCSoft v02-02 [16] to conduct simulations and reconstructions. The parameters of the incoming beams are simulated using the GUINEA-PIG package [17, 18]. The beam spectrum, including beamstrahlung and initial state radiation (ISR), is taken into account. In line with the current ILC design, the beam crossing angle of 14 mrad is taken into consideration. For the generation of Monte Carlo (MC) samples of the signal and SM background events, the WHIZARD 2.8.5 event generator [19, 20] is employed. The signal events were generated by employing the UFO model that was developed in [7], with 6 different values for dark neutrino mass $m_N = 95, 100, 105, 110, 115, 120 \text{ GeV}$. The parton shower and hadronization model is adopted from PYTHIA 6.4 [21]. To simulate the detector response, the generated events are passed through the ILD simulation [6] (model version ILD_l5_v02) implemented with the DD4HEP [22, 23] software package, which is based on Geant4 [24–26]. Event reconstruction is performed using the Marlin [27] framework. The PandoraPFA [28] algorithm is specifically employed for calorimeter clustering and the analysis of track and calorimeter information, following the particle flow

approach.

The samples used for the background are all SM processes (excluding ones with the Higgs boson) where two, four, and six fermions are produced. Additionally, processes where two quarks and one Higgs boson are produced (almost exclusively $e^+e^- \rightarrow ZH \rightarrow q\bar{q}H$) are included as background, including all possible SM decay modes of the Higgs. Each background can also be separated into leptonic (only leptons in the final state), semileptonic (leptons and hadrons in the final state) or hadronic (only hadrons in the final state) decay channels.

The three-fermion final state where the incoming electron or positron interacts with a photon was also investigated as a background. However, all simulated electron-gamma samples were excluded after the cuts applied (see further down) and are therefore not included in the background. The cross sections for the background processes are given in Table I.

Process	Abbreviation	Cross section $(-0.8, +0.3)$ [fb]	Cross section $(+0.8, -0.3)$ [fb]
2 fermion leptonic	2f_l	13 000	10 300
2 fermion hadronic	2f_h	77 300	45 700
4 fermion leptonic	4f_l	10 400	6 110
4 fermion semileptonic	4f_sl	19 200	2 840
4 fermion hadronic	4f_h	16 800	1 570
6 fermion	6f	1.28	0.26
$e^+e^- \rightarrow q\bar{q}H$	qqh	208	140
Signal (BR = 1%)	Signal	1.396	0.941

TABLE I: Cross sections of the various background processes [29]. For example, “2 fermion hadronic” means that there are two hadronic fermions produced in the final state, i.e., all SM processes (excluding processes involving the Higgs) of $e^+e^- \rightarrow q\bar{q}$. The signal cross section shows the case when the branching ratio is 1%.

The analysis for applying cuts were done with the ROOT C++/Python framework 6.28 [30] and Jupyter notebooks [31]. The machine learning model was developed with TMVA [32].

III. ANALYSIS

For each polarization scheme and each mass value of dark neutrino, the event selection and cuts applied to reduce the background were done in three stages: pre-selection, rectangular cuts, and a machine learning cut, explained in detail in the following subsections. As a preview of the analysis procedure a cut flow table of all the cuts applied and the number of events that pass each cut, separated for the different background categories, are shown in Table II. The table is an example of the cuts for a dark neutrino mass of 100 GeV, a joint branching ratio of 1%, beam polarization of $(+0.8, -0.3)$, and an integrated luminosity of 1 ab^{-1} .

Cut	Signal	Background	σ	2f_l	2f_h	4f_l	4f_sl	4f_h	6f	qqh
No cuts	941	66651497	0.12	10314870	45672588	6114301	2839022	1570051	260	140405
Pre-selection	831	12565351	0.23	5696748	979693	4109167	1739683	22431	194	17434
cut 1	769	1287215	0.68	70332	146740	897907	149918	15416	142	6759
cut 2	722	1025729	0.71	61382	49161	785129	120467	4506	132	4952
cut 3	708	434591	1.07	44787	22077	293992	67433	2031	74	4197
cut 4	665	24666	4.18	399	4093	1176	13462	1687	72	3777
cut 5	583	6919	6.73	0	1151	0	1234	1384	55	3094
cut 6	574	4487	8.07	0	544	0	666	648	19	2611
MVA cut	434	1162	10.87	0	52	0	26	79	6	999

TABLE II: Cut flow table for a dark neutrino mass of 100 GeV, a joint branching ratio of 1%, beam polarization of $(+0.8, -0.3)$ and an integrated luminosity of 1 ab^{-1} . The numbered cuts represent rectangular cuts, which are explained in more detail below. The column named σ is the signal significance in units of standard deviation σ .

A. Pre-selection

The final state of signal events consists of one charged lepton, one neutrino and four jets. The pre-selection is applied to reconstruct the basic information of the leptons and jets, as well as to properly pair them into W , Z , N_d and Higgs in each event, based on the signal

characteristics. The pre-selection will supply the necessary information for the next cuts. The procedure of pre-selection is briefly explained here.

Isolated leptons were first identified in each event using a pre-trained neural network by the IsolatedLeptonTagging algorithm in iLCSoft [27]. In this algorithm, the isolated leptons are required to have a momentum of at least 5 GeV. The neural network gives a numerical output for each particle of the event usually between 0 and 1 (though it can give a higher value, even up to 2), with a higher value meaning that a particle is more likely an isolated lepton. If the particle is a muon, it is required that the isolated lepton finder output is greater than 0.5, whereas if it is an electron, it is required to be greater than 0.2. Only a loose cut is applied on this parameter in the pre-selection not to remove signal and background events too early. Each event is then required to have at least one isolated lepton according to these criteria. For the signal, typically only one lepton fulfills this but there are occasionally ($< 1\%$) 2 or more leptons. In that case, the highest energy lepton is chosen as the isolated lepton.

The remaining particles in the event are clustered into four jets using the Durham jet clustering algorithm [33]. If this fails, the event is also rejected. The four jets are then paired with each other and classified as W jets or Z jets based on which pairing minimized

$$\chi^2 = \left(\frac{m_W - m_{12,jet}}{\Delta m_{W,jet}} \right)^2 + \left(\frac{m_Z - m_{34,jet}}{\Delta m_{Z,jet}} \right)^2. \quad (6)$$

Here, $m_W = 80.4$ GeV and $m_Z = 91.187$ GeV are the W and Z boson masses. $m_{12,jet}$, $m_{34,jet}$ are the reconstructed masses based on a certain pairing of jets and their 4-momenta. $\Delta m_{W,jet} = 5.3$ GeV, $\Delta m_{Z,jet} = 6.8$ GeV represent the mass resolutions of W and Z bosons. This is calculated by using MC truth information to identify which of the reconstructed jets originate from W or Z jets on this basis [34]. The mass distributions are shown in Figure 3 for $e^+e^- \rightarrow ZH \rightarrow q\bar{q} WW^* \rightarrow q\bar{q} q\bar{q} l\nu$ events. Since this process is the dominant background, it has the same final state and has very similar kinematics as the dark neutrino model, the W and Z mass resolutions are similar to signal events.

After the jet clustering and jet pairing, the W and charged lepton are grouped to form reconstructed N_d . The missing 4-momentum, calculated as the 4-momentum of initial state minus the total 4-momentum of all reconstructed visible particles in the final state, is reconstructed as the 4-momentum of ν . Then Higgs is reconstructed as sum of the 4-momenta of N_d and ν . After the pre-selection most of the hadronic background events are rejected, as

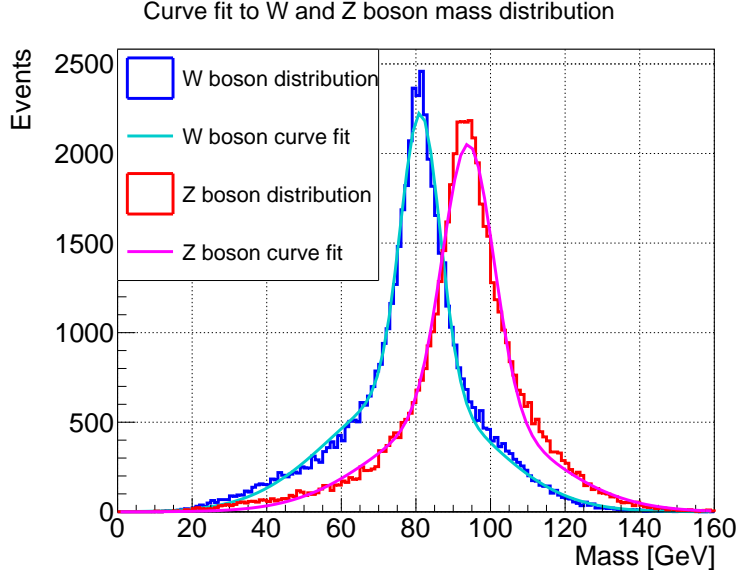


FIG. 3: Reconstructed mass distributions of the W and Z bosons, by pairing jets using MC truth information. The smooth lines are curve fits to the histograms.

they do not have an isolated lepton, and large portions of the leptonic backgrounds are also reduced, as they fail the 4-jet reconstruction; details shown in Table II.

B. Rectangular cuts

For the rectangular cuts, various observables were identified by comparing their distributions between signal and background events. Cut values were optimized to maximize the final signal significance after the rectangular cuts and the machine learning cut.

The first cut applied was a combination of missing energy and lepton energy. This was mainly to reduce the leptonic and semileptonic backgrounds, which have high energy leptons or neutrinos. As an example, the 2D distributions of the lepton energy (E_{lep}) and missing energy (E_{mis}) for the 4f_sl background and signal are shown in Figure 4. The plot (and all subsequent plots in this section) are for a beam polarization of $(+0.8, -0.3)$, dark neutrino mass of 100 GeV, and a branching ratio of 1% for the signal. The cut (cut 1) was set to $E_{lep}/50\text{GeV} + E_{mis}/100\text{GeV} < 1$. The results of all cuts shown in figures below, are the ones shown in Table II.

The second cut applied was on the isolated lepton finder output, which is required to be greater than 0.6 (cut 2). This cut is tighter than the loose cut applied by default in

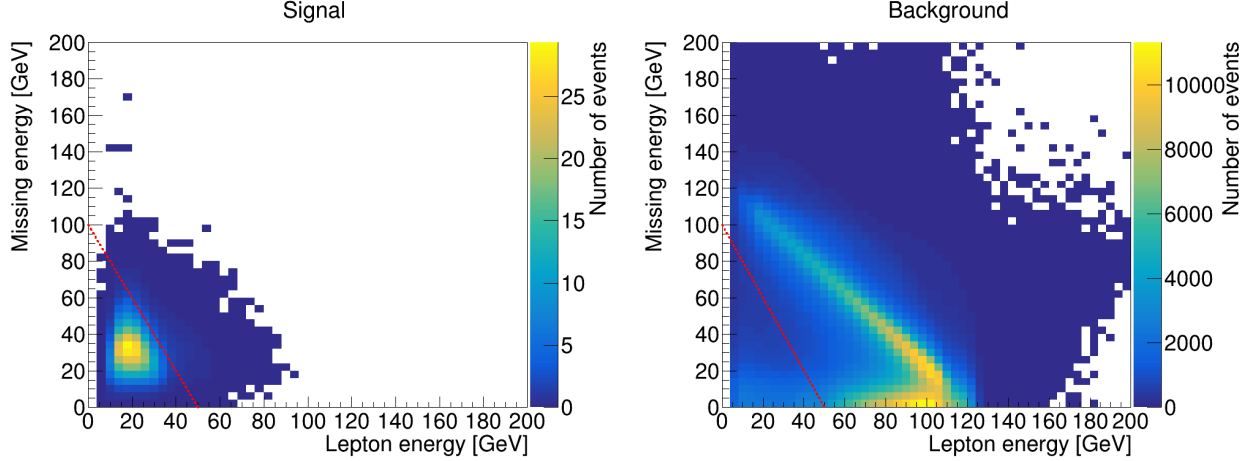


FIG. 4: 2D distributions of the signal and background for isolated lepton energy (x -axis) and missing energy (y -axis) for a beam polarization of $(+0.8, -0.3)$ and a dark neutrino mass of 100 GeV. The background distribution shown is the $4f_sl$ background, where the red line shows the cut that is applied. The number of events shown for the signal is for a branching ratio of 1% but the distribution does not change for other branching ratios.

the isolated lepton finder algorithm in the pre-selection. This cut mainly suppresses further the hadronic backgrounds ($2f_h$ and $4f_h$) where a lepton from a jet was mistagged as an isolated lepton. The distributions for the signal and background, as well as the cut value is shown in Figure 5. Note that the events shown are only the events passing the previous cut(s). This applies to all the upcoming similar plots in this section.

Next, the 4-jet combined invariant mass is required to be between 160 and 220 GeV (cut 3), which reduces both the hadronic (at the high-mass region) and semi-leptonic / leptonic (at the low-mass region) backgrounds. The distributions of the 4-jet invariant mass is shown in Figure 6 for the signal and the total background events.

The fourth cut applied is on the Durham jet distance $y_{4\rightarrow 3}$, calculated as

$$y_{4\rightarrow 3} = \min_{i,j} \left\{ \frac{2 \min\{E_i, E_j\}^2 (1 - \cos \theta_{ij})}{E_{vis}^2} \right\}, \quad (7)$$

where E_i is the energy of jet i , θ_{ij} is the angle between jets i and j , and E_{vis} is the total energy of the four jets. This jet distance is used for the jet clustering and the pair of jets that give the smallest jet distance are combined, hence the use of min in the equation above. This clustering is performed multiple times until there are only four jets left, and $y_{4\rightarrow 3}$ is the minimum jet distance at this stage. By requiring $y_{4\rightarrow 3} > 0.004$ (cut 4), this can therefore

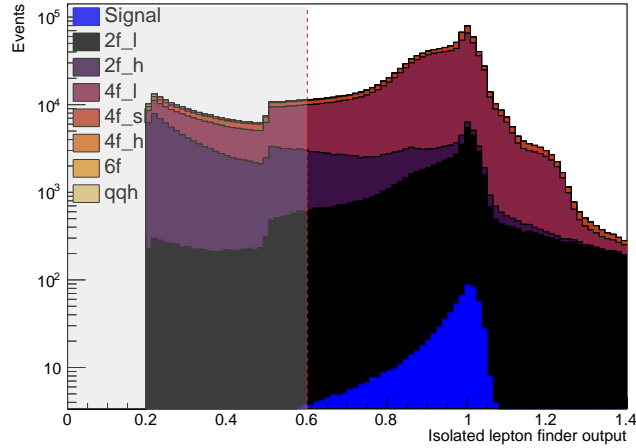


FIG. 5: The distributions of the isolated lepton finder output for the signal and background, where different colors indicate different background processes. The same beam polarization and dark neutrino mass is shown as in Figure 4. The distributions are properly normalized according to the corresponding cross sections. The red vertical line shows the cut value and the grey region is the region that is rejected. A logarithmic scale is used on the y -axis.

help filter out semi-leptonic and leptonic background events, as shown in Figure 7.

The fifth cut applied is that any jet in the event must have at least four particles (cut 5). This cut further reduces the semi-leptonic and leptonic backgrounds, as shown in Figure 8.

The final rectangular cut is on the missing momentum. This is highly dependent on the dark neutrino mass and a different cut value is therefore used for each mass point. The missing momentum for each mass point is shown in Figure 9 (left). Both lower and upper bound cuts are used to reduce all types of backgrounds. The signal and background distributions can be seen in Figure 9, right plot. In this case, for a dark neutrino mass of 100 GeV, the missing momentum is required to be between 10 and 45 GeV (cut 6).

As shown in Table II after all the rectangular cuts, the background is dominated by the irreducible qqh background, followed by remaining 4-fermion hadronic and semi-leptonic background. The signal over background ratio (S/B) is already improved by 4 orders of magnitude, from $1/10^5$ in the beginning to $1/10$. The same cut variables are used for both beam polarizations but the cut values are optimized separately, as the background and signal differs for the two beam polarizations. Generally, the cuts for $(+0.8, -0.3)$ are looser, as

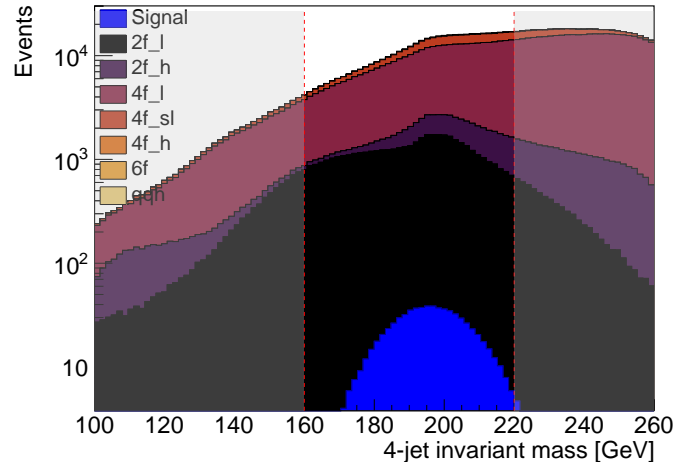


FIG. 6: The distributions of 4-jet invariant mass for the signal and background. The figure format is the same as in Figure 5.

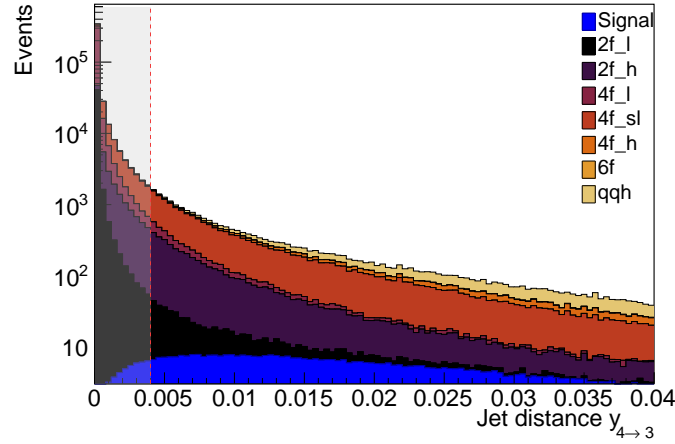


FIG. 7: The distributions of the jet distance $y_{4 \rightarrow 3}$ for the signal and background. The figure format is the same as in Figure 5.

the background is lower. Two cuts that were highly dependent on the dark neutrino mass, specifically the first and last rectangular cuts, were optimized and tuned for each mass point.

C. Machine learning

The signal and background events that passed the rectangular cuts were further filtered through a boosted decision tree (BDT) using the TMVA framework [32]. One BDT was

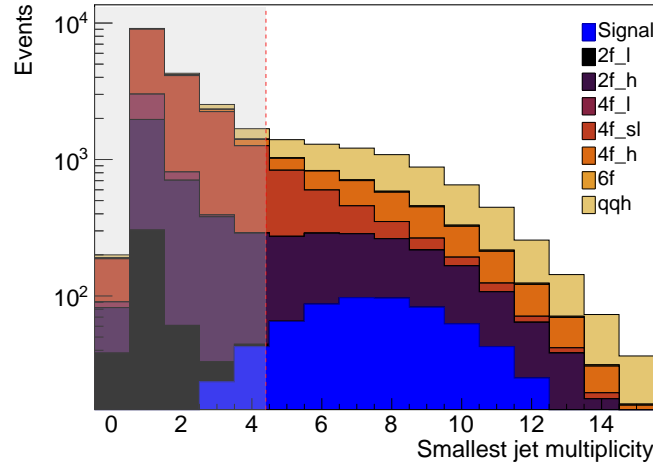


FIG. 8: The distributions of the smallest number of particles in the jets of each event. for the signal and background. The figure format is the same as in Figure 5. The histogram bins are centered at each integer.

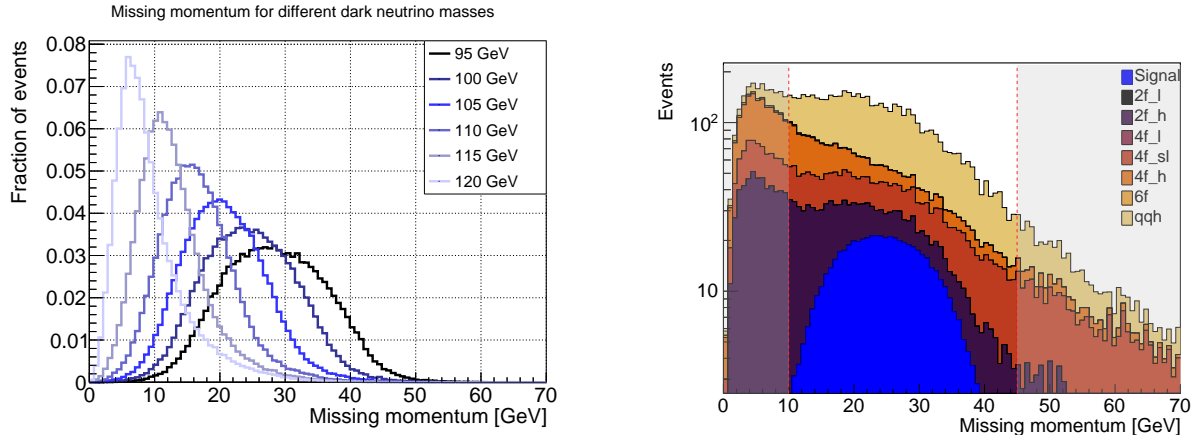


FIG. 9: The distributions of the missing momentum. The left plot shows each dark neutrino mass. The left plot shows the signal and background for a dark neutrino mass of 100 GeV in the same format as Figure 5.

trained for each mass point and beam polarization. In total, 13 input parameters were passed to the BDT. The input parameters are listed below.

- The lepton and missing energies
- 4-jet combined momentum
- The angle between the lepton and the closest jet

- $\cos \theta_l, \cos \theta_\nu, \cos \theta_Z, \cos \theta_{N_d}$, where θ is the production angle (in the lab frame) of the particle indicated by the subscript. The particles are the isolated lepton, reconstructed neutrino, Z boson and dark neutrino, respectively
- The cosine of the lepton helicity angle in the dark neutrino rest frame
- The reconstructed Higgs, Z boson, and W boson masses
- The corrected reconstructed dark neutrino mass

The formula for the corrected reconstructed dark neutrino mass is $m(N_d) - m_W + m_{W_0}$, where m_W is the reconstructed W boson mass and $m_{W_0} = 80.4$ GeV is the truth central value of the W boson mass. This corrected dark neutrino mass has better resolution than that directly reconstructed from the lepton and two jets from W since the largest uncertainty from the jet reconstruction can mostly cancel out. Distributions of some example input parameters for the signal and background are shown in Figure 10. The rest of the input parameters to the BDT can be found in the appendix. One example of the BDT output distributions is shown in Figure 11, where it is validated that the BDT was not overfitted. Here, it can clearly be seen that the BDT output distribution is nearly identical for the training (dots) and test (filled) events. The Kolmogorov-Smirnov test also gives a high value (above 0.05) which quantitatively shows that the distributions are similar to each other. A final cut is applied to the BDT output which further improves the S/B by a factor of 3, as shown in Table II, and after the final cut the background contribution is completely dominated by qqh process.

It is worth pointing out that by comparing the truth and reconstructed information we found that the jet clustering and jet pairing to distinguish jets from Z and jets from W is not perfect. Instead, jet constituents can originate from both Z and W bosons, which result in a bias in the jet momentum. This is discussed in further detail in the appendix.

IV. RESULTS

The analysis above illustrated mostly for one benchmark scenario, is carried out for each of the six values of dark neutrino mass from 95 GeV to 120 GeV, each of the two beam polarization schemes and each of the two lepton channels (e and μ). The final BDT cut to

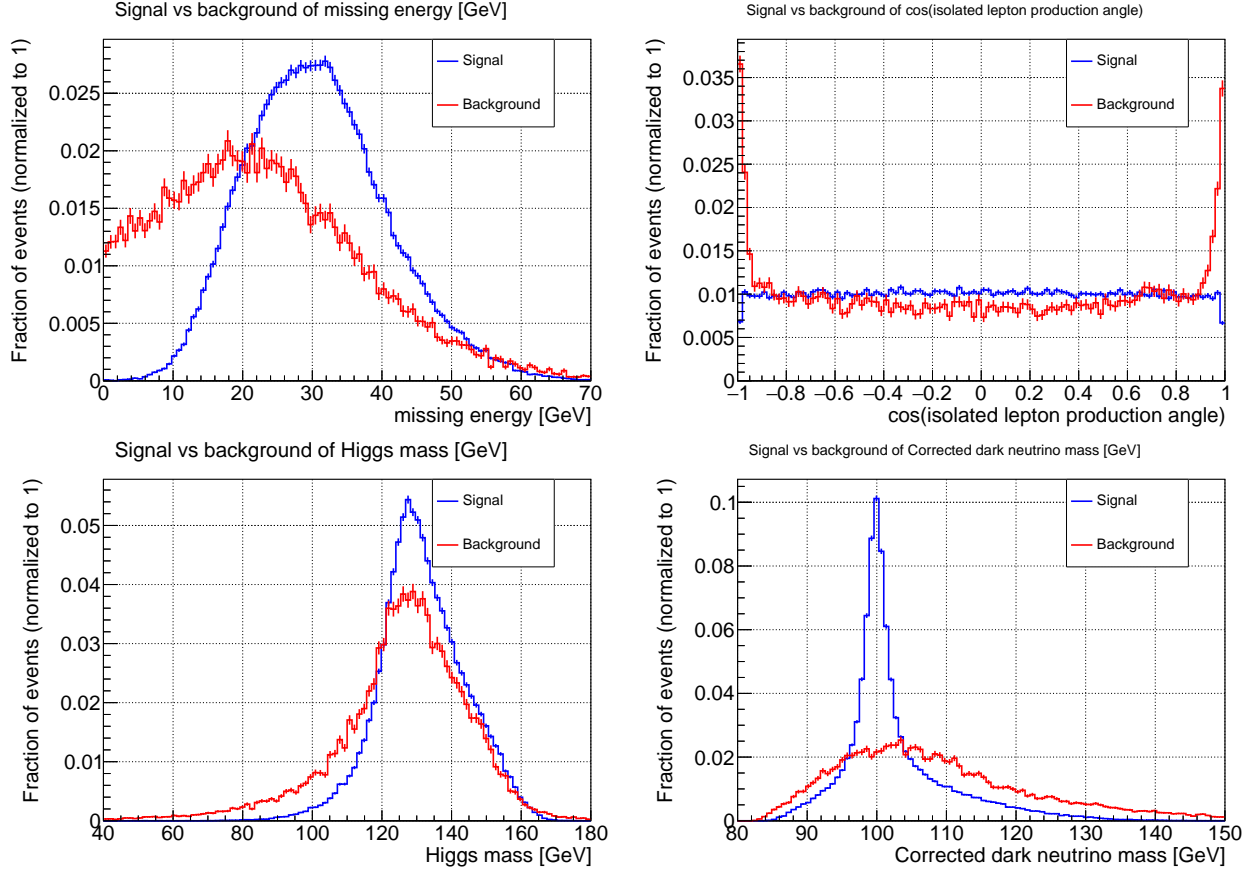


FIG. 10: Distributions of a few input parameters to the BDT for the signal and background events, with the format as same as in e.g., Figure 5, except that there is no grey region indicated. As in the previous figures, a dark neutrino mass of 100 GeV and a beam polarization of $(+0.8, -0.3)$ is shown. From top left to bottom right with the first row first: missing energy, cosine of lepton production angle in the lab frame, the Higgs mass, and the corrected dark neutrino mass.

maximize the signal significance also depends on the value of joint branching ratio as shown in Figure 12 for a range of branching ratios from 0.01% to 10%. The final significance for each branching ratio and dark neutrino mass is then calculated by combining the contribution from two beam polarization schemes and two lepton channels. This combination is calculated as

$$\sigma_{final} = \sqrt{\sum_i \sigma_i^2} \quad (8)$$

where i iterates over the four $(2 \cdot 2)$ possible combinations of lepton channels and beam polarizations.

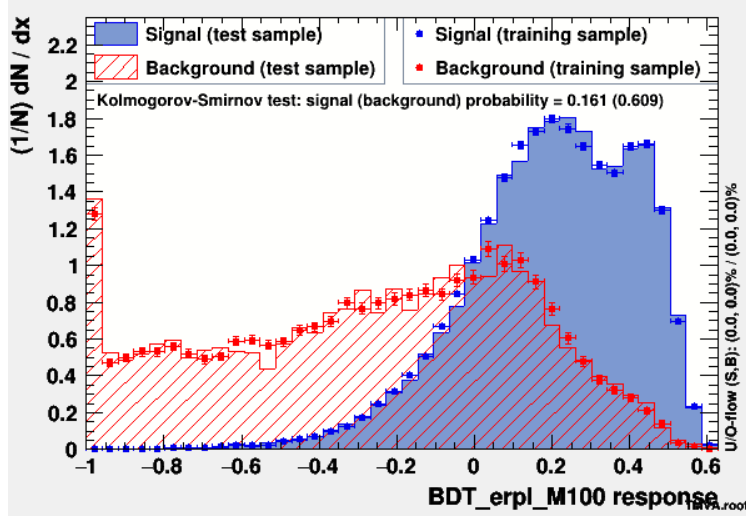


FIG. 11: The distributions of BDT output for a BDT trained on the signal and background events when the dark neutrino mass is 100 GeV and the beam polarization is $(+0.8, -0.3)$. The filled histograms show the signal and background events for the test data, while the dotted histograms show the training data.

To better visualize the remained signal and background events, we separately trained a BDT without using the corrected dark neutrino mass as one input variable, applied a cut on that BDT output, and then plotted the distributions of the corrected dark neutrino mass, as shown in Figure 13. If the branching ratio is as large as 1%, a sharp resonance from the dark neutrino signal events would be clearly visible on top of the background events.

We are now ready to give our model-independent final result in terms of the signal significance for searching the dark neutrinos at the ILC250 as a function of the dark neutrino mass and the joint branching ratio of $BR(H \rightarrow \bar{\nu} N_d) \cdot BR(N_d \rightarrow lW)$. The result is shown in Figure 14, where the red line indicates the exclusion limit for 2σ significance and the green line indicates the discovery potential for 5σ significance. We can see in Figure 14 that the significance is almost identical regardless of dark neutrino mass, with a slight decrease close to 100 GeV. This is most likely due to the background distribution, which has a peak close to 100-105 GeV (see Figure 13). This means that it is more difficult for the BDT to discriminate the signal from the background, since the mass peaks overlap. As a consequence of this, the significance is highest at 120 GeV, since this is the farthest away from the background mass peak. As a conclusion the exclusion limit (discovery potential) for the joint branching ratio is about 0.1% (0.3%), nearly independent of the dark neutrino mass given the mass range

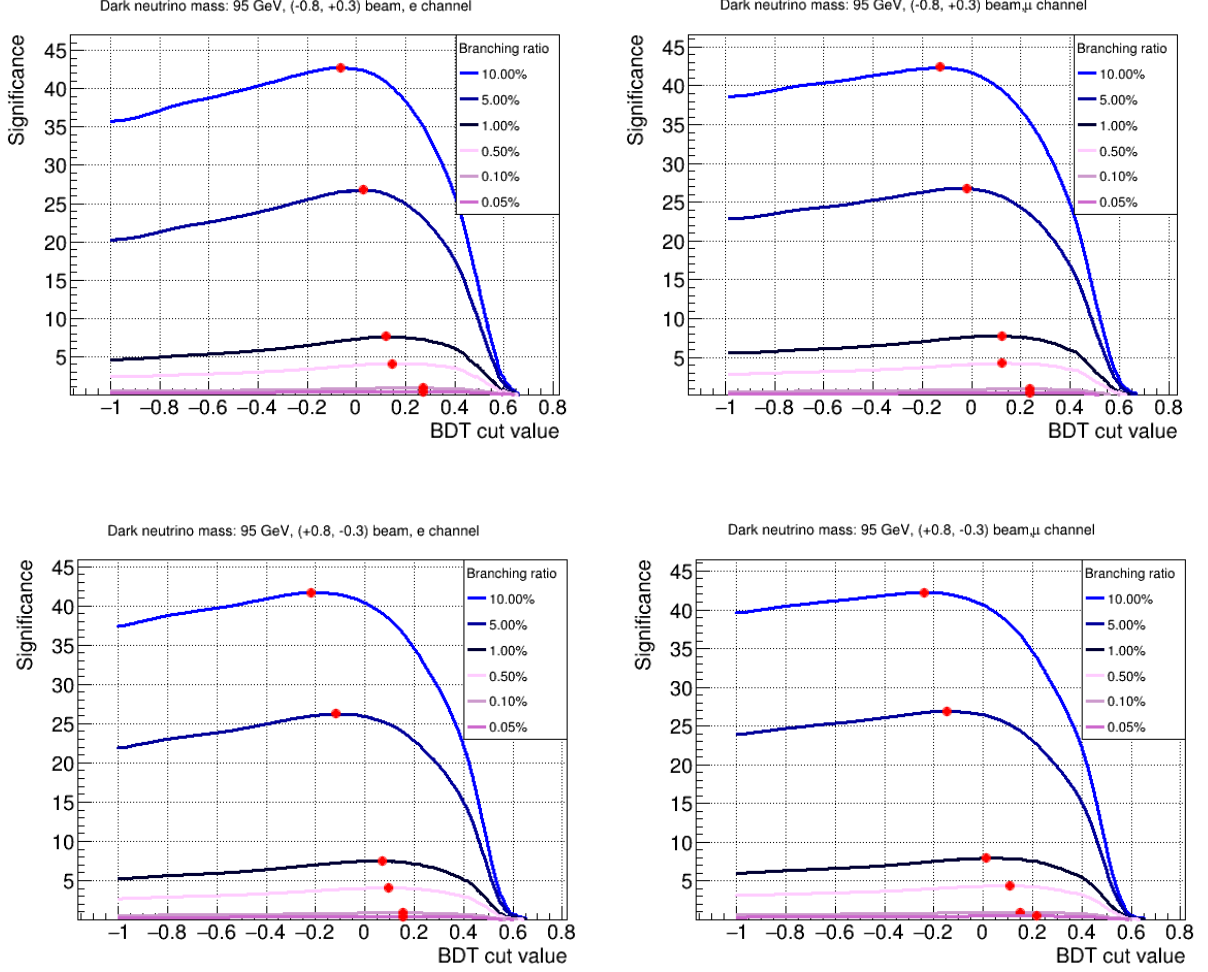


FIG. 12: Examples of significance curves as function of the BDT cut value for different values of branching ratio. All plots are for dark neutrino masses of 95 GeV, with the top and bottom row being for $(-0.8, +0.3)$ and $(+0.8, -0.3)$ beam polarization respectively. The left (right) column of plots show the electron (muon) channel. Red dots indicate the location of maximum significance for different branching ratios where corresponding final cut is applied. The significance curves for other dark neutrino masses and beam polarizations typically have a similar shape.

between m_Z and m_H .

The model-independent results can be cast into constraints on the two free model parameters, dark neutrino mass m_N and mixing parameter $|\varepsilon_{id}|^2$, as introduced in Section 1, using Equation 5. Note that in this interpretation, the branching ratio $BR(H \rightarrow \nu \bar{N}_d + \bar{\nu} N_d) =$

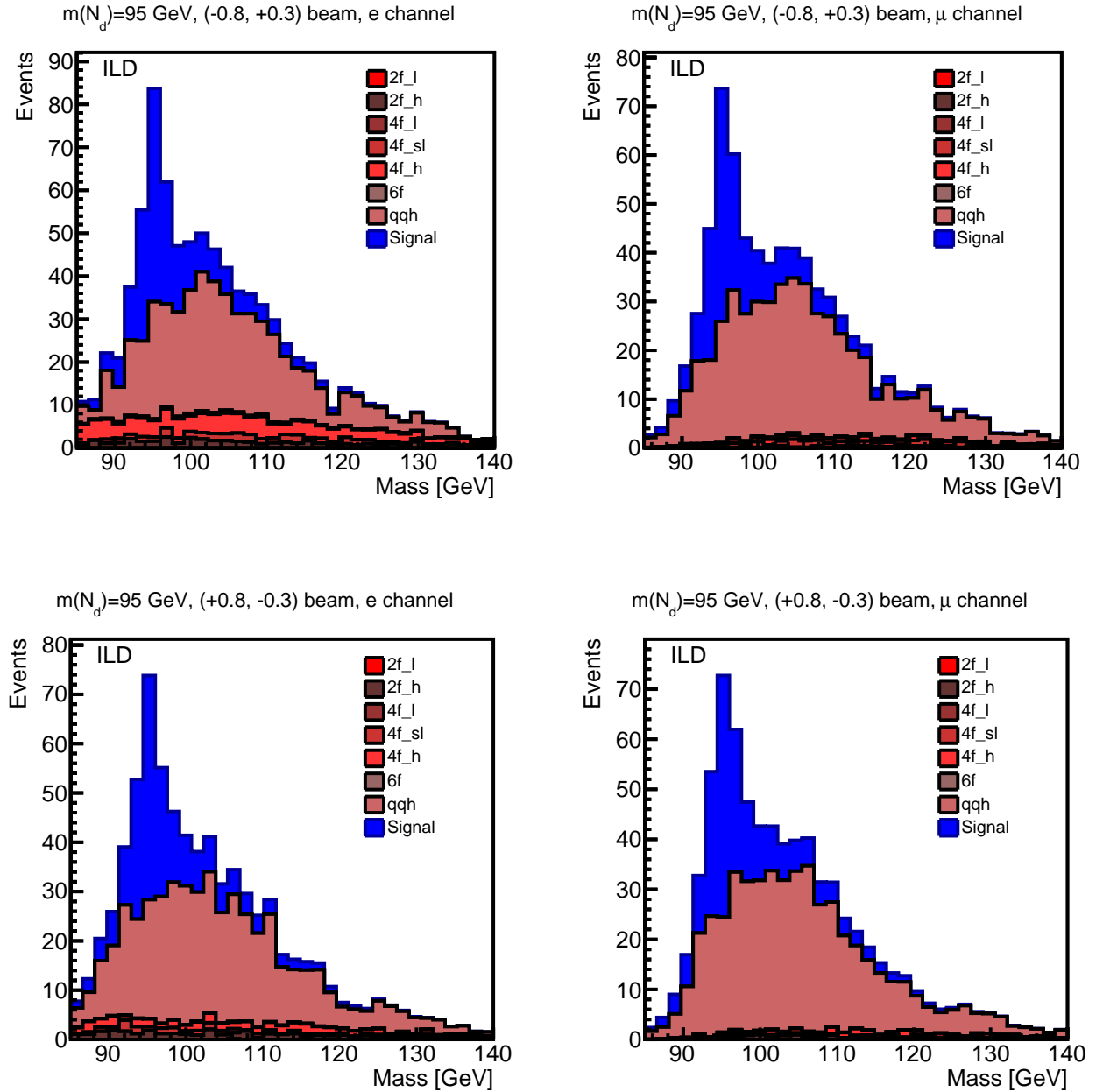


FIG. 13: Examples of mass distributions after all cuts, with a branching ratio of 1%. The final BDT cut does not use the neutrino mass as input for this figure. The order of the plots is the same as in Figure 12. The backgrounds are categorized based on if a process result in 2 leptons (2f_l), 2 quarks (2f_h), 4 leptons (4f_l), 2 leptons and 2 quarks (4f_sl), 4 quarks (4f_h), 6 fermions (6f), or 2 quarks and a Higgs boson (qqh). The signal is marked with blue.

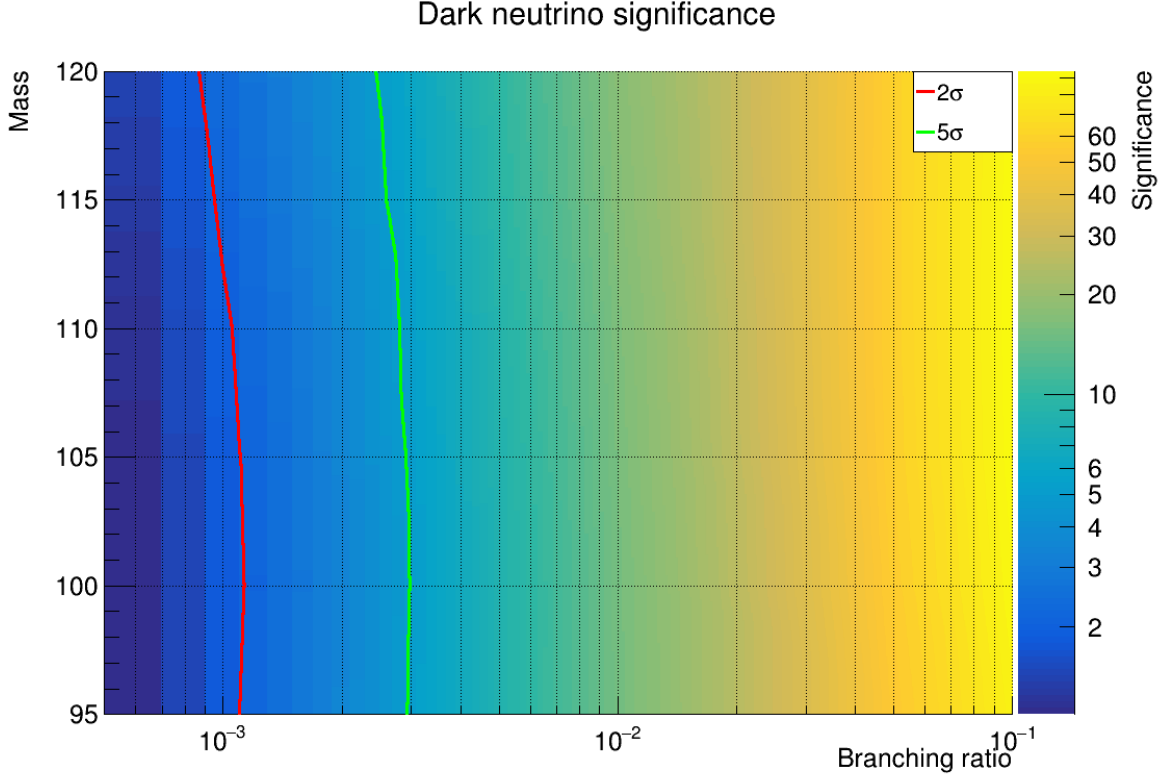


FIG. 14: Exclusion plot as a function of branching ratio $BR(H \rightarrow \nu N_d)BR(N_d \rightarrow lW)$ (x axis) and dark neutrino mass (y axis). The color indicates the significance of detecting this channel. The red curve indicates where the significance is 2σ , i.e., the exclusion limit, whereas the green line shows the 5σ limit, i.e., the limit for discovery. Every parameter value to the right of the red (green) line can be excluded (discovered). Note that a log scale is used on the x and z axis. The significance is interpolated in between the tested mass points and branching ratios and may not be completely accurate.

$2BR(H \rightarrow \nu \bar{N}_d)$ is used, i.e., a factor of 2 is multiplied to the branching ratio in Equation 5. The limits are calculated separately for the electron and muon channels. The constraints from this study, together with constraints imposed by previous studies mentioned above are shown in Figure 15. The exclusion limits from current constraints are taken from [35, 36]. We can see that the exclusion limit on $|\varepsilon_{id}|^2$ down to 10^{-4} can be reached at the ILC250, in the dark neutrino mass region between Z mass and Higgs mass, which is about 1-order of magnitude improvement over the current constraint.

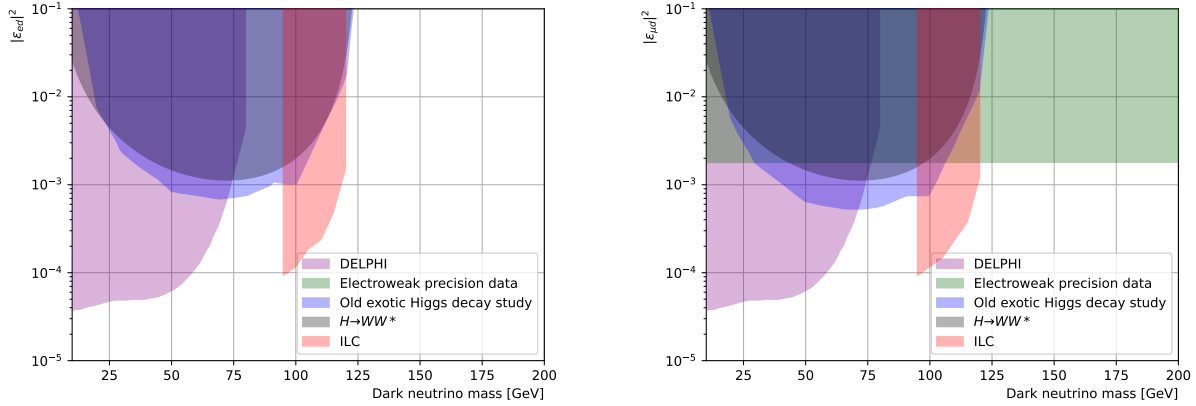


FIG. 15: The exclusion curves for the mixing angle between the dark neutrino and the electron neutrino (left plot) and the muon neutrino (right plot). The x -axis is the dark neutrino mass while the y -axis is the squared amplitude of the mixing angle. The dark green region shows the constraints from measurements of the SM neutrino mixing angles, the purple region shows the constraints from searches by DELPHI at LEP, the blue region shows the results from [8], and the gray region shows the region where the $BR(H \rightarrow \nu N_d) > 0.05$. The red region shows the new results from this study using simulated ILC data. Note that the y -axis is a logarithmic scale. For the red contour, the exclusion curve is linearly interpolated between each simulated mass point (95 - 120 GeV, 5 GeV apart).

A. Discussion for potential improvement

As mentioned earlier one source of error in this analysis is the jet clustering and jet pairing. This was e.g., evident in the distribution of the lepton helicity angle in the dark neutrino rest frame (see e.g., Figure 16). Improving this by using better jet clustering algorithms and/or a more sophisticated method for jet pairing could improve the measurements of the 4-momenta of the jets, which in turn improves the precision of the W and Z bosons reconstruction, and consequently of the dark neutrino and Higgs boson reconstruction. It is therefore potentially of great help to improve jet clustering algorithms for future experiments and analyses that focus on precision measurements.

Another potential improvement to this study is on the correction of the dark neutrino mass. Currently, a simple correction was used by subtracting the W boson mass and adding

a constant, which evidently worked well for this study, since the W boson 4-momentum measurement was the main source of error. However, one could also employ techniques such as kinematic fitting to correct for errors more accurately in the W boson 4-momentum, which could improve mass resolution of the dark neutrino mass even more. This is also closely related to the jet clustering error mentioned above.

To further improve the sensitivity to the dark neutrino, other decay channels can be investigated. This includes the τ decay channel (i.e., $H \rightarrow \nu_\tau N_d \rightarrow \nu_\tau \tau q \bar{q}$) as well as two other W and Z boson decay channels. However, the other two decay channels are likely to provide little sensitivity. The semi-leptonic decay, i.e., a leptonic decay of the W or Z boson and a hadronic decay of the other one, would likely be difficult to discriminate from the background. This is because the final state contains two neutrinos which makes it difficult to reconstruct W and/or the Z boson and thus the dark neutrino and Higgs. Additionally, there are two jets in the final state which has a large background. The other fully leptonic decay with three neutrinos and three leptons will likely have a very small background. However, reconstructing the dark neutrino or any of the W , Z , and H bosons will be almost impossible. Still, this decay channel was more sensitive than the hadronic decay channel for the LHC [8], though this does not mean that it will be the same for ILC, since the background characteristics are different. It is therefore totally possible that this and other decay channels would have sizable contributions to the significance.

V. SUMMARY

The sensitivity of the ILC for detecting heavy dark neutrinos through exotic Higgs decays was investigated. The $e^+e^- \rightarrow ZH \rightarrow q\bar{q} \nu N_d \rightarrow q\bar{q} \nu lW \rightarrow q\bar{q} \nu l q\bar{q}$ channel was studied, for the first time to our knowledge based on full detector simulations. The analysis was performed at 250 GeV center-of-mass energy for two different beam polarization schemes, and for six dark neutrino masses between m_Z and m_H . The SM background with 2, 4, 6-fermion final states as well as $q\bar{q}H$ processes were all considered in the analysis. Events were filtered through a pre-selection, a set of rectangular cuts, and finally a machine learning cut. The cuts were separately optimized for all combinations of beam polarizations and dark neutrino masses, though the pre-selection was the same for all of them. The background contribution turns out to be very important, and only after all the dedicated event selection

cuts the signal over background ratio could be improved from $O(1/10^5)$ to $O(1)$. For all masses simulated, the dominating background after all cuts was from the SM Higgs decay process $H \rightarrow WW^* \rightarrow q\bar{q}l\nu$. The final significance achieved was around 2σ for a branching ratio of $BR(H \rightarrow \nu N_d) \cdot BR(N_d \rightarrow lW) = 0.1\%$, while 5σ is reachable at a branching ratio of 0.3% . The significance is almost unchanged for different masses. Interpreting these results for dark neutrino models results in constraints on the mixing angle $|\varepsilon_{id}|^2$ between SM neutrinos and the dark neutrino of levels down to 10^{-4} , which is a factor of 10 improvement from previous constraints.

ACKNOWLEDGEMENT

We would like to thank Teresa Núñez, Alberto Ruíz and Kiyotomo Kawagoe for constructive discussions and suggestions during the ILD internal review process. We also would like to thank Hitoshi Murayama and Robert McGehee for providing helpful theory guidance, ILD Monte Carlo Team in particular Hiroaki Ono and Ryo Yonamine for producing the common SM background samples, Krzysztof Mękała and Jürgen Reuter for pointing out the proper UFO model file for Whizard to generate signal events, and Kay Hidaka, Daniel Jeans, Shigeki Matsumoto, Satoshi Shirai, Taikan Suehara for discussions at various local meetings. This research was supported by the Sweden-Japan foundation and “Insamlingsstiftelsen för internationellt studentutbyte vid KTH”.

-
- [1] G. Aad *et al.* (ATLAS), Observation of a new particle in the search for the Standard Model Higgs boson with the ATLAS detector at the LHC, Phys. Lett. B **716**, 1 (2012), arXiv:1207.7214 [hep-ex].
 - [2] S. Chatrchyan *et al.* (CMS), Observation of a New Boson at a Mass of 125 GeV with the CMS Experiment at the LHC, Phys. Lett. B **716**, 30 (2012), arXiv:1207.7235 [hep-ex].
 - [3] A. Aryshev, T. Behnke, M. Berggren, J. Brau, N. Craig, A. Freitas, F. Gaede, S. Gessner, S. Gori, C. Grojean, *et al.*, The international linear collider: Report to snowmass 2021 (2023), arXiv:2203.07622 [physics.acc-ph].

- [4] The International Linear Collider Technical Design Report - Volume 2: Physics, (2013), arXiv:1306.6352 [hep-ph].
- [5] E. Hall, T. Konstandin, R. McGehee, H. Murayama, and G. Servant, Baryogenesis from a dark first-order phase transition, *Journal of High Energy Physics* **2020**, 10.1007/jhep04(2020)042 (2020).
- [6] T. Behnke, J. E. Brau, P. N. Burrows, J. Fuster, M. Peskin, M. Stanitzki, Y. Sugimoto, S. Yamada, and H. Yamamoto, The international linear collider technical design report - volume 4: Detectors (2013), arXiv:1306.6329 [physics.ins-det].
- [7] K. Mękała, J. Reuter, and A. F. Żarnecki, Heavy neutrinos at future linear e^+e^- colliders, *JHEP* **06**, 010, arXiv:2202.06703 [hep-ph].
- [8] A. Das, P. B. Dev, and C. Kim, Constraining sterile neutrinos from precision higgs data, *Physical Review D* **95**, 10.1103/physrevd.95.115013 (2017).
- [9] A. Pich, Precision Tau Physics, *Prog. Part. Nucl. Phys.* **75**, 41 (2014), arXiv:1310.7922 [hep-ph].
- [10] P. Abreu *et al.* (DELPHI collaboration), Search for neutral heavy leptons produced in Z decays, *Zeitschrift für Physik C Particles and Fields* **74**, 57 (1997).
- [11] A. M. Sirunyan *et al.* (CMS), Search for heavy neutral leptons in events with three charged leptons in proton-proton collisions at $\sqrt{s} = 13$ TeV, *Phys. Rev. Lett.* **120**, 221801 (2018), arXiv:1802.02965 [hep-ex].
- [12] G. Aad *et al.* (ATLAS), Search for heavy neutral leptons in decays of W bosons produced in 13 TeV pp collisions using prompt and displaced signatures with the ATLAS detector, *JHEP* **10**, 265, arXiv:1905.09787 [hep-ex].
- [13] G. Aad *et al.* (ATLAS), A detailed map of higgs boson interactions by the ATLAS experiment ten years after the discovery, *Nature* **607**, 52 (2022).
- [14] P. Bambade *et al.*, The International Linear Collider: A Global Project, (2019), arXiv:1903.01629 [hep-ex].
- [15] This scenario is for simplicity, slightly different with the standard scenario in which the total integrated luminosity is shared also by a small fraction for other two beam polarization schemes. The difference would not affect significantly our results.
- [16] iLCSoft, ilcsoft documentation, <https://github.com/iLCSoft/ilcsoftDoc> (2017).

- [17] D. Schulte, *Study of Electromagnetic and Hadronic Background in the Interaction Region of the TESLA Collider*, Ph.D. thesis, Hamburg U. (1997), presented on Apr 1997.
- [18] D. Schulte, Beam-Beam Simulations with GUINEA-PIG, 5th International Computational Accelerator Physics Conference (1998).
- [19] W. Kilian, T. Ohl, and J. Reuter, Whizard—simulating multi-particle processes at LHC and ILC, *The European Physical Journal C* **71**, 1 (2011).
- [20] M. Moretti, T. Ohl, and J. Reuter, O’mega: An optimizing matrix element generator, arXiv preprint hep-ph/0102195 (2001).
- [21] T. Sjöstrand, S. Mrenna, and P. Skands, PYTHIA 6.4 physics and manual, *Journal of High Energy Physics* **2006**, 026 (2006).
- [22] M. Frank, F. Gaede, C. Grefe, and P. Mato, Dd4hep: A detector description toolkit for high energy physics experiments, *Journal of Physics: Conference Series* **513**, 022010 (2014).
- [23] M. Frank, F. Gaede, N. Nikiforou, M. Petric, and A. Sailer, Ddg4 a simulation framework based on the dd4hep detector description toolkit, *Journal of Physics: Conference Series* **664**, 072017 (2015).
- [24] S. Agostinelli, J. Allison, K. Amako, J. Apostolakis, H. Araujo, P. Arce, M. Asai, D. Axen, S. Banerjee, G. Barrand, *et al.*, Geant4—a simulation toolkit, *Nuclear Instruments and Methods in Physics Research Section A: Accelerators, Spectrometers, Detectors and Associated Equipment* **506**, 250 (2003).
- [25] J. Allison, K. Amako, J. Apostolakis, P. Arce, M. Asai, T. Aso, E. Bagli, A. Bagulya, S. Banerjee, G. Barrand, *et al.*, Recent developments in Geant4, *Nuclear Instruments and Methods in Physics Research Section A: Accelerators, Spectrometers, Detectors and Associated Equipment* **835**, 186 (2016).
- [26] J. Allison, K. Amako, J. Apostolakis, H. Araujo, P. A. Dubois, M. Asai, G. Barrand, R. Capra, S. Chauvie, R. Chytrcek, *et al.*, Geant4 developments and applications, *IEEE Transactions on nuclear science* **53**, 270 (2006).
- [27] F. Gaede, Marlin and lccd—software tools for the ilc, *Nuclear Instruments and Methods in Physics Research Section A: Accelerators, Spectrometers, Detectors and Associated Equipment* **559**, 177 (2006), proceedings of the X International Workshop on Advanced Computing and Analysis Techniques in Physics Research.

- [28] M. Thomson, Particle flow calorimetry and the PandoraPFA algorithm, Nuclear Instruments and Methods in Physics Research Section A: Accelerators, Spectrometers, Detectors and Associated Equipment **611**, 25 (2009).
- [29] J. Tian *et al.* (ILD), Generator meta data, [Online; Accessed 2023-07-20].
- [30] CERN, ROOT - an object oriented framework for large scale data analysis - version 6.28 (2023).
- [31] M. Beg, J. Taka, T. Kluyver, A. Konovalov, M. Ragan-Kelley, N. M. Thiery, and H. Fangohr, Using Jupyter for reproducible scientific workflows, Computing in Science & Engineering **23**, 36 (2021).
- [32] A. Hoecker, P. Speckmayer, J. Stelzer, J. Therhaag, E. von Toerne, and H. Voss, TMVA: Toolkit for Multivariate Data Analysis, PoS **ACAT**, 040 (2007), arXiv:physics/0703039.
- [33] Y. Dokshitzer, G. Leder, S. Moretti, and B. Webber, Better jet clustering algorithms, Journal of High Energy Physics **1997**, 001 (1997).
- [34] To identify which jet corresponded to which boson, the reconstructed constituent particles in each jet were linked to their corresponding MC truth particle, and by traversing the tree of interactions it could be determined if a certain jet constituent particle originated from a W or Z boson. The scalar energy sum of all constituent particles originating from a Z and W boson respectively was calculated. If most of the energy came from the Z boson, the jet was classified as a Z jet and likewise for W jets. If more than two jets were classified as either Z or W jets, the event was ignored. After each jet was classified as a W or Z jet, the jet pair 4-momenta were added and the reconstructed masses were computed. The mass resolution for each particle was then set as the standard deviation of the mass distribution, when performing a fit of a normal distribution to the mass distributions.
- [35] P. D. Bolton, F. F. Deppisch, and P. B. Dev, Neutrinoless double beta decay versus other probes of heavy sterile neutrinos, Journal of High Energy Physics **2020**, 10.1007/jhep03(2020)170 (2020).
- [36] P. D. Bolton, F. F. Deppisch, and P. B. Dev, Plots and data - sterile neutrino constraints v1 documentation (2020).

VI. APPENDIX

A. Investigation of error in angles

One problem encountered when selecting input parameters for the BDT was with the lepton angle distribution in the dark neutrino rest frame. When comparing the MC truth distribution with the reconstructed one, there is a slight shift towards negative angles for reconstructed angles (see Figure 16). This can be explained by incorrect jet pairing and errors in the jet clustering. Since the Z boson is more massive than the W boson, in general there will be more energy in the Z boson jets than the W boson ones. All jets are however soft due to the low center-of-mass energy and since the produced particles (Higgs, dark neutrino etc) have a high mass. This makes it difficult for the jet clustering algorithm to correctly determine which particle should belong to which jet, and many particles originating from the Z boson can be misclassified as belonging to W bosons and vice versa. Furthermore, when performing the jet pairing, it is also possible for jets to incorrectly be assigned to the wrong boson, which further increases this error. As a consequence of this, the reconstructed W boson will sometimes have slightly higher energies and/or p_T than MC truth. This is shown in Figure 17. We also see that the W bosons with high p_T are the ones that contribute to an excess in negative helicity angles, as shown in Figure 18. This therefore further supports our theory. To increase the accuracy of future analyses and collider experiments, improved jet clustering algorithms are therefore important.

B. Additional figures

All 1D parameter distributions of the input parameters to the BDT are shown below. This only shows the distributions for a signal with a dark neutrino mass of 100 GeV and a beam polarization of $(+0.8, -0.3)$. Note that the y -axis has been normalized to only include the number of events. In reality, the signal histogram is much smaller relative to the background.

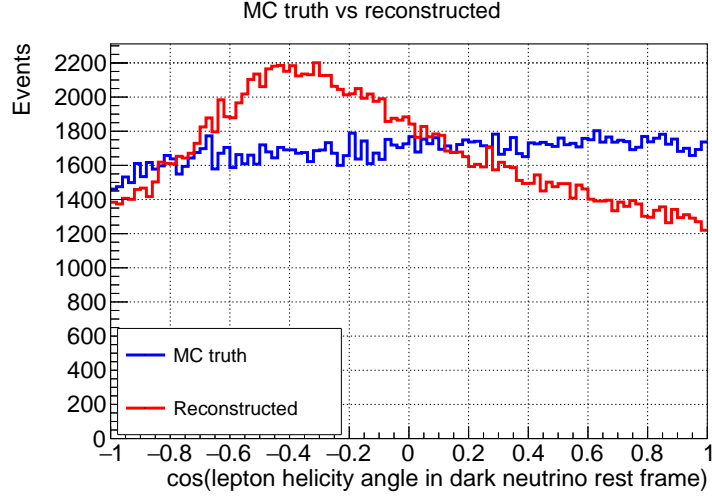


FIG. 16: Distributions of the cosine of the lepton helicity angle in the dark neutrino rest frame. The blue (red) histogram shows the MC truth (reconstructed) angular distribution. The y -axis shows the number of simulated events, without taking any cross section into account and is therefore arbitrary. The data shown is for a dark neutrino mass of 110 GeV and a beam polarization of $(-0.8, +0.3)$ but the same pattern can be seen for all other signal events.

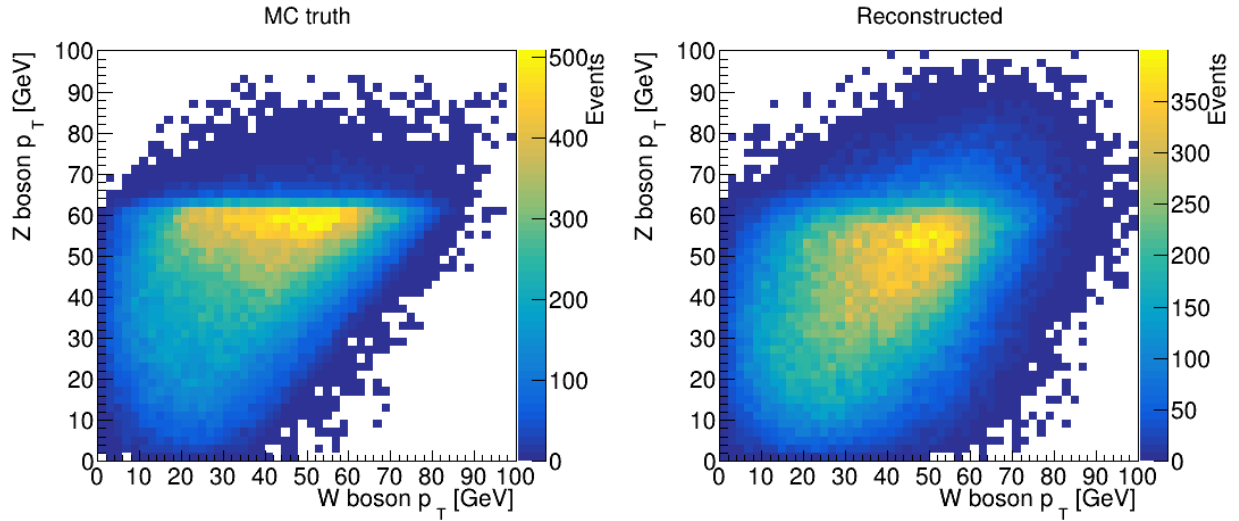


FIG. 17: 2D distributions of the W boson p_T (x -axis) vs Z boson p_T (y -axis). The left plot shows the MC truth distribution, while the right plot shows the reconstructed values. One can see that the concentrated cluster in the MC truth has been more spread out in the reconstructed version, with more values of higher W boson p_T and either lower or higher Z boson p_T .

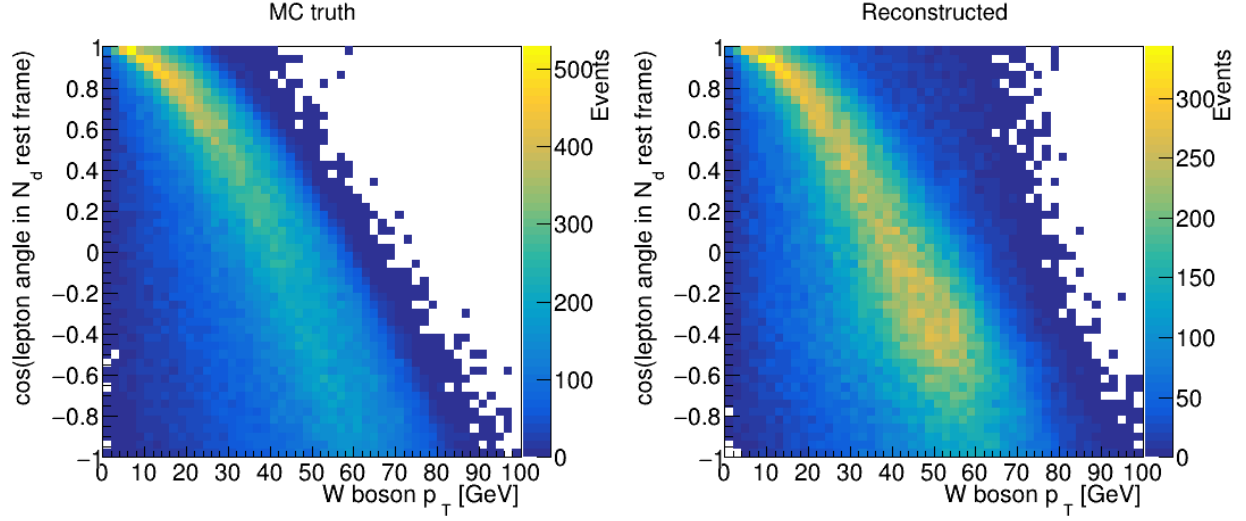


FIG. 18: 2D distributions of the W boson p_T (x -axis) vs lepton helicity angle (y -axis). The format is the same as in Figure 17. One can see that the number of high- p_T events have increased for reconstructed events and that these events typically appear for negative angles.

C. Separate results for electron and muon channels

The significance for discovery is shown for both the electron and muon decay channel separately, i.e., $N_d \rightarrow e^\pm W^\mp$ and $N_d \rightarrow \mu^\pm W^\mp$, in Figure 20. The electron/muon separation is done by using the reconstructed particles and identifying them as electrons or muons.

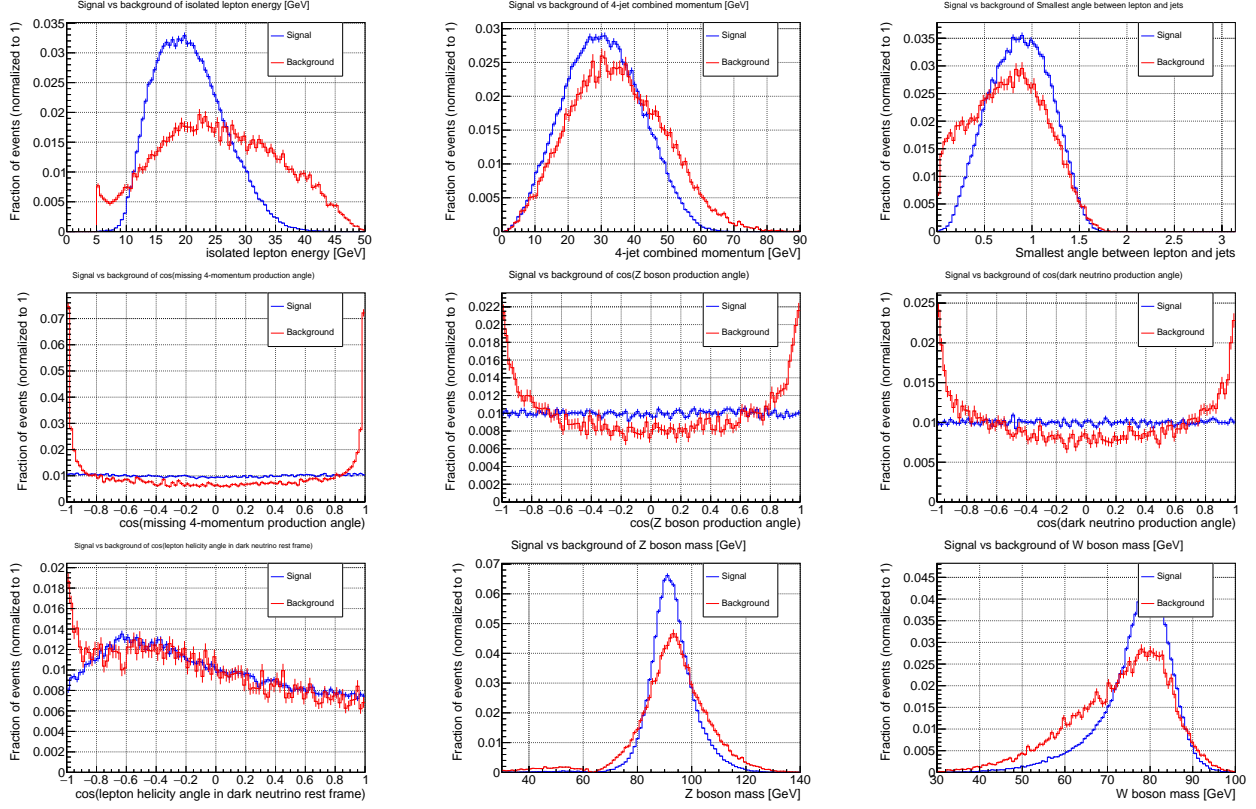


FIG. 19: Distirbutions of the BDT input parameters not shown in Figure 10. The figure format is the same as in Figure 10.

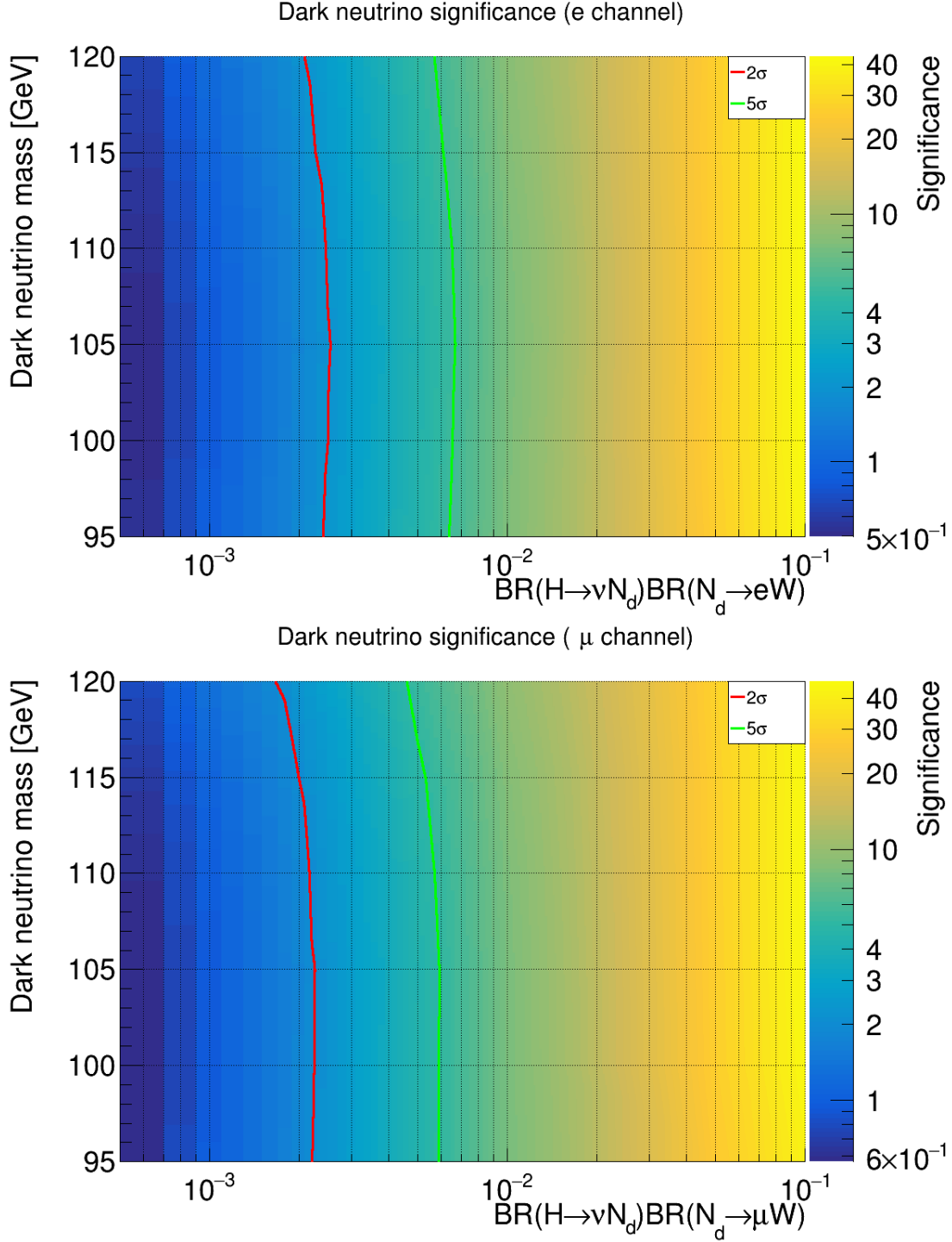


FIG. 20: Exclusion plot as a function of branching ratio $BR(H \rightarrow \nu N_d)BR(N_d \rightarrow l W)$ (x axis) and dark neutrino mass (y axis) for the two lepton channels. The top plot shows the electron channel ($N_d \rightarrow e^\pm W^\mp$) and the bottom plot shows the muon channel ($N_d \rightarrow \mu^\pm W^\mp$). The figure format is the same as in Figure 14.